Contribution from the Department of Applied Molecular Science, Institute for Molecular Science, Myodaiji, Okazaki 444, Japan, and Department of Chemistry, Faculty of Science, Kyushu University, Hakozaki, Higashiku, Fukuoka 812, Japan

Temperature-Dependent Crystallographic Studies on Ferric Spin-Crossover Complexes with Different Spin-Interconversion Rates

Hiroki Oshio,*,† Koshiro Toriumi,† Yonezo Maeda,‡ and Yoshimasa Takashima‡

Received February 13, 1991

Crystallographic studies of $[Fe(acpa)_2]X$ (Hacpa = *N*-(1-acetyl-2-propylidene)(2-pyridylmethyl)amine; X = BPh_4 (tetraphenylborate) and PF_6 (hexafluorophosphate)) have been done at several temperatures (120, 202, 247, and 311 K for the BPh_4^- salt and 120, 205, and 290 K for the PF_6^- salt). Temperature dependences of the magnetic susceptibilities show that both compounds undergo gradual spin transitions between high-spin ($^6A_{1g}$) and low-spin ($^2T_{2g}$) states, and 85.2% at 320 K and 97.8% at 290 K of the spin transitions to the high-spin state are observed for the BPh_4^- and the PF_6^- salts, respectively. ^{57}Fe Mössbauer spectra at 78 and 310 K for both compounds consist of a single quadrupole doublet corresponding to the low- and high-spin states. Within the spin transition temperature range, Mössbauer spectra of the PF_6^- salt consist of a superposition of the high- and low-spin species, while the BPh_4^- salt shows only one broad quadrupole doublet with isomer shift and quadrupole splitting parameters in proportion to the fraction of the high- or low-spin species. The Mössbauer spectra imply a rapid spin interconversion rate for the BPh_4^- salt compared with the reciprocal of the Mössbauer lifetime (10^{-7} s) and also indicate that the BPh_4^- salt interconverts its spin state faster than the PF_6^- salt. The BPh_4^- and PF_6^- salts crystallize in triclinic and monoclinic space groups, respectively, and show no drastic structural change such as order–disorder transformations when the temperature is varied. Crystallographic studies at different temperatures, however, reveal remarkable changes of coordination bond lengths going along with the spin-state interconversion (ΔFe–O$_{av}$ = 0.026 Å, ΔFe–N(pyridine)$_{av}$ = 0.130 Å, and ΔFe–N(imine)$_{av}$ = 0.112 Å for the BPh_4^- salt and ΔFe–O = 0.051 Å, ΔFe–N(pyridine) = 0.168 Å, and ΔFe–N(imine) = 0.143 Å for the PF_6^- salt). The smaller bond length changes for the BPh_4^- salt are responsible for a smaller activation energy, ΔE_a, between the high- and low-spin states, hence the faster spin interconversion rate for the BPh_4^- salt than for the PF_6^- salt. Crystal data: X = BPh_4^-, 120 K, triclinic, $P\bar{1}$, Z = 2, a = 12.784 (3) Å, b = 13.290 (4) Å, c = 11.776 (4) Å, α = 93.35 (3)°, β = 102.29 (2)°, γ = 98.37 (2)°, refinement to R = 0.038 and R_w = 0.047; X = BPh_4^-, 202 K, triclinic, $P\bar{1}$, Z = 2, a = 12.868 (4) Å, b = 13.383 (3) Å, c = 11.820 (4) Å, α = 93.38 (2)°, β = 102.37 (2)°, γ = 98.17 (2)°, refinement to R = 0.033 and R_w = 0.039; X = BPh_4^-, 247 K triclinic, $P\bar{1}$, Z = 2, a = 12.918 (3) Å, b = 13.458 (2) Å, c = 11.800 (3) Å, α = 92.23 (1)°, β = 102.25 (2)°, γ = 98.30 (2)°, refinement to R = 0.036 and R_w = 0.040; X = BPh_4^-, 311 K, triclinic, $P\bar{1}$, Z = 2, a = 12.982 (3) Å, b = 13.592 (2) Å, c = 11.791 (3) Å, α = 92.87 (1)°, β = 101.77 (2)°, γ = 98.74 (1)°, refinement to R = 0.042 and R_w = 0.044; X = PF_6^-, 120 K, monoclinic, $P2/a$, Z = 2, a = 13.626 (2) Å, b = 9.847 (1) Å, c = 10.169 (1) Å, β = 111.93 (1)°, refinement to R = 0.045 and R_w = 0.049; X = PF_6^-, 205 K, monoclinic, $P2/a$, Z = 2, a = 13.644 (2) Å, b = 9.874 (1) Å, c = 10.240 (1) Å, β = 111.09 (1)°, refinement to R = 0.054 and R_w = 0.065; X = PF_6^-, 290 K, monoclinic, $P2/a$, Z = 2, a = 13.674 (1) Å, b = 9.911 (1) Å, c = 10.325 (1) Å, β = 110.43 (1)°, refinement to R = 0.039 and R_w = 0.059.

Introduction

Since Cambi and co-workers found an anomalous magnetic behavior, called spin crossover, in tris(*N,N*-dialkyldithiocarbamato)iron(III) complexes,[1] the spin-crossover phenomena in iron(II)[2–15] and iron(III)[16–19] complexes have been extensively studied. The spin-crossover complexes are classified into two groups depending on the spin-transition behaviors: (i) a "spin-transition (ST) type", where type of complex shows that the spin transition between high- and low-spin states occurs abruptly or discontinuously within a few Kelvin; (ii) a "spin-equilibrium (SE) type", where the spin transition in this type of complex occurs gradually over a wide temperature range. Both types of spin-crossover systems have been found in iron(II) and iron(III) systems. There are theoretical arguments and experimental data that can clarify why such spin-crossover behaviors are different in each system. Kambara pointed out that the strengths of a Jahn–Teller coupling between d electrons and local distortions[20] and of an intermolecular coupling between intramolecular distortions and lattice strain[21,22] play important roles in determining the spin-crossover behavior. On the other hand, heat capacity measurements for the different spin-crossover systems have shown that the total entropy changes ΔS accompanying spin transition are 36.74, 36.19, 48.78, and 50.59 J K^{-1} mol^{-1} for $[Fe^{III}(3\text{-}OMeSalEen)_2]PF_6$,[23] $[Fe^{III}(acpa)_2]PF_6$,[24] $[Fe^{II}(phen)_2(NCS)_2]$,[10,11] and $[Fe^{II}(2\text{-}pic)_3]Cl_2\cdot EtOH$,[25] respectively, where 3-OMeSalEen is the Schiff base condensate of 3-methoxysalicylaldehyde and *N*-(3-aminopropyl)aziridine and 2-pic is 2-aminopyridine. These values are much larger than those of a change in the spin manifold between the low- and high-spin states: ΔS = 9.13 (=R ln 3) and 13.38 J K^{-1} mol^{-1} (=R ln 5) for iron(III) and iron(II) systems, respectively. The extra entropy change has been ascribed to the change in the phonon systems and to order–disorder phenomena of the solvent molecules or counteranions. The kinetic mechanism of the spin transition has been explained by a domain model. It has been pointed out that the estimated domain size (number of molecules in a domain) for the ST type system (95 for $[Fe(phen)_2(NCS)_2]$[10]) is larger than that of the SE type system (5 for $[Fe^{III}(acpa)_2]PF_6$[24]). These results suggest that the ST type complexes are strongly coupled with the lattice phonon system.

† Institute for Molecular Science.
‡ Kyushu University.

(1) Cambi, L.; Cagnasso, A. *Atti Accad. Naz. Lincei, Cl. Sci. Fis. Mat. Nat. Rend.* **1931**, *13*, 809.
(2) Adler, P.; Wiehl, L.; Meissner, E.; Köhler, C. P.; Spiering, H.; Meissner, E.; Gütlich, P. *J. Phys. Chem. Solids* **1987**, *48*, 517.
(3) Sorai, M.; Ensling, J.; Gütlich, P. *Chem. Phys. Lett.* **1976**, *18*, 199.
(4) Köppen, H.; Müller, E. W.; Köhler, C. P.; Spiering, H.; Meissner, E.; Gütlich, P. *Chem. Phys. Lett.* **1982**, *91*, 348.
(5) Gütlich, P. *Struct. Bonding* **1981**, *44*, 83.
(6) Kōnig, E.; Ritter, G.; Kulshreshtha, S. K. *Chem. Rev.* **1985**, *85*, 219.
(7) Kōnig, E.; Madeja, K. *Inorg. Chem.* **1967**, *6*, 48.
(8) Kōnig, E.; Ritter, G.; Irler, W.; Goodwin, H. A. *J. Am. Chem. Soc.* **1980**, *102*, 4681.
(9) Kōnig, E.; Ritter, G.; Kulshreshtha, S. K.; Nelson, S. M. *J. Am. Chem. Soc.* **1983**, *105*, 1924.
(10) Sorai, M.; Seki, S. *J. Phys. Soc. Jpn.* **1972**, *33*, 575.
(11) Sorai, M.; Seki, S. *J. Phys. Chem. Solids* **1974**, *34*, 555.
(12) Maeda, M.; Takashima, Y.; Nishida, Y. *Bull Chem. Soc. Jpn.* **1976**, *49*, 2427.
(13) Greenaway, A. M.; Sinn, E. *J. Am. Chem. Soc.* **1978**, *100*, 8080.
(14) Greenaway, A. M.; O'Connor, C. J.; Schrock, A.; Sinn, E. *Inorg. Chem.* **1979**, *18*, 2692.
(15) Katz, B. A.; Strouse, C. E. *J. Am. Chem. Soc.* **1979**, *101*, 6214.
(16) Hadad, M. S.; Lynch, M. W.; Federer, W. D.; Hendrickson, D. N. *Inorg. Chem.* **1981**, *20*, 123.
(17) Federer, W. D.; Hendrickson, D. N. *Inorg. Chem.* **1984**, *23*, 3870.
(18) Timken, M. D.; Strouse, C. E.; Soltis, S. M.; Daverio, S. R.; Hendrickson, D. N.; Abdel-Mawgoud, A. M.; Wilson, S. A. *J. Am. Chem. Soc.* **1986**, *108*, 395.
(19) Sim, G.; Sinn, E.; Petty, R. H.; Merrill, C. L.; Wilson, L. J. *Inorg. Chem.* **1981**, *20*, 213.
(20) Kambara, T. *J. Chem. Phys.* **1979**, *70*, 4199.
(21) Sasaki, T.; Kambara, T. *J. Chem. Phys.* **1981**, *74*, 3472.
(22) Kambara, T. *J. Chem. Phys.* **1981**, *74*, 4557.
(23) Sorai, M.; Hendrickson, D. N. Personal communication.
(24) Sorai, M.; Maeda, Y.; Oshio, H. *J. Phys. Chem. Solids* **1990**, *51*, 941.
(25) Kaji, K.; Sorai, M. *Thermochim. Acta* **1985**, *88*, 185.

0020-1669/91/1330-4252$02.50/0

On the other hand, some systems of the SE type interconvert their spin states faster than the reciprocal of the ^{57}Fe Mössbauer lifetime (10^{-7} s). If the spin interconversion is slower than the Mössbauer lifetime, two sets of quadrupole doublets corresponding to the high- and low-spin states can be obtained in the Mössbauer spectra. In the case of much faster spin interconversion than the Mössbauer lifetime, the two sets of doublets can no longer be resolved and only one quadrupole doublet with quadrupole splitting and isomer shift parameters corresponding to the fraction of each spin state can be observed. If the spin interconversion rate is comparable to the Mössbauer lifetime, Mössbauer spectra show broadened quadrupole doublet lines, so-called relaxation spectra. Recently, the fast spin interconversion phenomena have been recognized in iron(III) complexes with N_4O_2 Schiff-base ligands by Hendrickson et al.,[16,17,18,26] Nishida et al.,[27] Murray et al.,[28] and us[29-31] and also in iron(III) dithio-,[32] monothio-,[33] and diselenocarbamates[34] and an iron(III) porphyrin $[Fe(OEP)X_2]ClO_4$ (OEP = octaethylporphyrin; X = 2-methylimidazole, 3,5-dichloropyridine) by Scheidt et al.[35,36] It is evident from the experimental results that the spin-interconversion rates depend on subtle solid-state effects such as counterions and ligand-substitution effects. However, only a few crystallographic studies at different temperatures have been available.[18,28,37,38] Hendrickson et al.[18] suggested that the change in the electron-transfer rate is coupled to the onset of a dynamic motion of a solvent molecule in the lattice; dynamic disorder in the lattice leads to rapid spin-interconversion rates, and static order leads to slow rates. It is unfortunate that the factors determining the spin-interconversion rate are still ambiguous.

SE type complexes $[Fe(acpa)_2]X$ (X = BPh_4, PF_6) have been proved to have different spin-interconversion rates by Mössbauer spectroscopic studies.[31] The spin-interconversion rate of the BPh_4^- salt is faster than that of the PF_6^- salt and the reciprocal of the ^{57}Fe Mössbauer lifetime (10^{-7} s). Since these complexes have the same ligand and each counterion causes the different spin-interconversion rate, they are suitable systems for studying the origin of the rapid spin interconversion with respect to a dynamic feature of the structure. In this paper, X-ray crystallographic studies on $[Fe(acpa)_2]X$ (X = BPh_4, PF_6) at different temperatures are presented and the possible origin of the rapid spin transition is discussed.

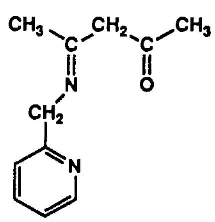

Hacpa

Experimental Section

Compound Preparation. $[Fe(acpa)_2]X$ (X = BPh_4, PF_6) were prepared by the method described elsewhere.[31] Single crystals suitable for X-ray analyses were grown by slow evaporation of a CH_2Cl_2 solution.

Physical Measurements. Freshly prepared samples were used for physical measurements. Variable magnetic susceptibility measurements down to liquid-nitrogen temperature were carried out by the conventional Faraday method. The instrument was calibrated with $HgCo(NCS)_4$, diamagnetic corrections were made by the use of Pascal's constant,[39] and effective magnetic moments were calculated by using the formula $\mu_{eff} = 2.83(\chi_M T)^{1/2}$, where χ_M is a corrected molar magnetic susceptibility.

^{57}Fe Mössbauer measurements were made on a constant-acceleration spectrometer described previously.[29] All isomer shifts are reported with respect to the center of the spectrum of an iron foil at 295 K. All spectra were fitted to Lorentzian line shapes.

Structure Determinations. Crystals of $[Fe(acpa)_2]BPh_4$ and $[Fe(acpa)_2]PF_6$ form as dark blue tablets. Each crystal suitable for X-ray analysis was attached to the end of a glass fiber. Data collections were made at various temperatures (120, 202, 247, and 311 K for the BPh_4^- salt and 120, 205, and 290 K for the PF_6^- salt) on a Rigaku AFC5 diffractometer equipped with a variable-temperature apparatus based on a cold N_2 gas stream method. The temperatures were measured after the data collections with a thermocouple mounted at the position of the crystal. The fluctuation in temperature was less than 1 K. The same crystal was used for measurements at different temperatures except for the measurement of PF_6^- salt at 290 K. Intensity data were obtained by use of an ω-2θ scan by using graphite-monochromated Mo Kα radiation: With $|F_o| > 3\sigma(F_o)$, 4644, 4983, 4992, and 3197 reflections at 120, 202, 247, and 311 K, respectively, for X = BPh_4^- and 2949 and 3035 reflections at 120 and 205 K, respectively, for X = PF_6^- were considered "observed" and "used" for the structure solution and least-squares refinements. The intensities were corrected for Lorentz and polarization factors but not for extinction. Accurate lattice constants were determined by a least-squares refinement based on 50 reflections ($25° < 2\theta < 30°$) measured on the diffractometer. The structures were solved by a conventional heavy-atom method and refined by a block-diagonal least-squares technique with anisotropic thermal parameters for non-H atoms

Table I. Crystal and Refinement Data for $[Fe(acpa)_2]BPh_4$

	temp, K 120	202	247	311
formula	$C_{46}H_{46}BFeN_4O_2$			
fw	753.552			
space group	$P\bar{1}$, triclinic			
a, Å	12.784 (3)	12.868 (4)	12.918 (3)	12.982 (3)
b, Å	13.290 (4)	13.383 (3)	13.458 (2)	13.592 (2)
c, Å	11.776 (4)	11.820 (4)	11.800 (3)	11.791 (3)
α, deg	93.35 (3)	93.38 (2)	92.23 (1)	92.87 (1)
β, deg	102.29 (2)	102.37 (2)	102.25 (2)	101.77 (2)
γ, deg	98.37 (2)	98.17 (2)	98.30 (2)	98.74 (1)
V, Å^3	1939.0 (9)	1959.8 (10)	1978.7 (7)	2006.2 (7)
Z	2	2	2	2
ρ_c, g cm^{-3}	1.290	1.277	1.265	1.247
μ(Mo Kα), cm^{-1}	4.473	4.425	4.383	4.323
R^a	0.038	0.033	0.036	0.042
R_w^b	0.047	0.039	0.040	0.044

$^a R = \sum(|F_o| - |F_c|)/\sum|F_o|$. $^b R_w = [\sum w(|F_o| - |F_c|)^2/\sum w|F_o|^2]^{1/2}$; $w = 1/\sigma^2(|F_o|)$.

Table II. Crystal and Refinement Data for $[Fe(acpa)_2]PF_6$

	temp, K 120	205	290^a
formula	$C_{22}H_{26}F_6FeN_4O_2P$		
fw	579.284		
space group	$P2/a$, monoclinic		
a, Å	13.626 (2)	13.644 (2)	13.674 (1)
b, Å	9.847 (1)	9.874 (1)	9.911 (1)
c, Å	10.169 (1)	10.240 (1)	10.325 (1)
β, deg	111.93 (1)	111.09 (1)	110.43 (1)
V, Å^3	1265.7 (3)	1287.2 (4)	1311.3 (2)
Z	2	2	2
ρ_c, g cm^{-3}	1.520	1.494	1.467
μ(Mo Kα), cm^{-1}	7.518	7.393	7.275
R	0.045	0.054	0.039
R_w	0.049	0.065	0.059

^{a} Reference 43.

(26) Timken, M. D.; Abdel-Mawgoud, A. M.; Hendrickson, D. N. *Inorg. Chem.* **1986**, *25*, 160.
(27) Nishida, Y.; Oshio, S.; Kida, S. *Bull. Chem. Soc. Jpn.* **1977**, *50*, 199.
(28) Kennedy, B. J.; McGrath, A. C.; Murray, K. S.; Skelton, B. W.; White, A. H. *Inorg. Chem.* **1987**, *26*, 483.
(29) Oshio, H.; Maeda, Y.; Takashima, Y. *Inorg. Chem.* **1983**, *22*, 2684.
(30) Oshio, H.; Kitazaki, K.; Mishiro, J.; Kato, N.; Maeda, Y.; Takashima, Y. *J. Chem. Soc., Dalton Trans.* **1987**, 1341.
(31) Maeda, Y.; Tsutsumi, N.; Takashima, Y. *Inorg. Chem.* **1984**, *23*, 2440.
(32) Merrithew, P. B.; Rasmussen, P. G. *Inorg. Chem.* **1972**, *11*, 325.
(33) Kunze, K. R.; Perry, D. L.; Wilson, L. J. *Inorg. Chem.* **1977**, *16*, 594.
(34) DeFilipo, D.; Depalano, P.; Diaz, A.; Steffe, S.; Trogu, E. F. *J. Chem. Soc., Dalton Trans.* **1977**, 1566.
(35) Greiger, D. K.; Lee, Y. J.; Scheidt, W. R. *J. Am. Chem. Soc.* **1984**, *106*, 6339.
(36) Scheidt, W. R.; Osvath, S. R.; Lee, Y. J.; Reed, C. A.; Shaevitz, B.; Gupta, G. P. *Inorg. Chem.* **1989**, *28*, 1591.
(37) Maeda, Y.; Oshio, H.; Toriumi, K.; Takashima, Y. *J. Chem. Soc., Dalton Trans.* **1991**, 1227.
(38) Gallois, B.; Real, J.; Hauw, C.; Zarembowitch, J. *Inorg. Chem.* **1990**, *29*, 1152.
(39) Bourdeauz, E. A.; Mulay, L. N. *Theory and Application of Molecular Paramagnetism*; John Wiley: New York, 1976; p 491.

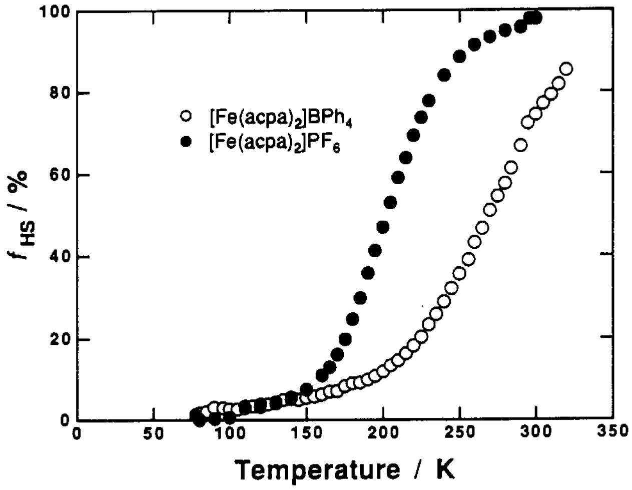

Figure 1. Temperature dependences of the high-spin fraction of $[Fe(acpa)_2]X$: (i) X = BPh_4 (○); (ii) X = PF_6 (●).

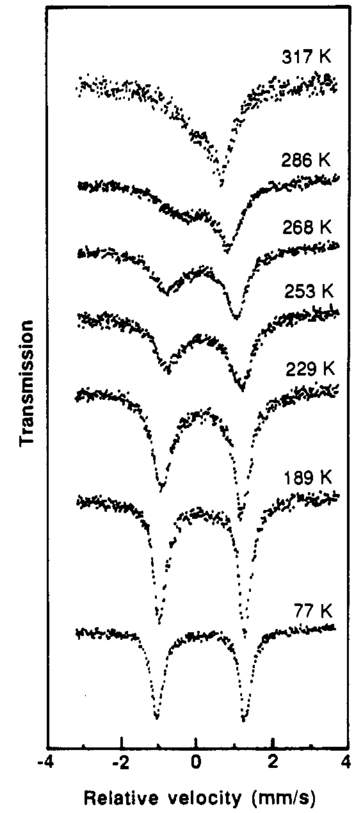

Figure 2. Mössbauer spectra of $[Fe(acpa)_2]BPh_4$.

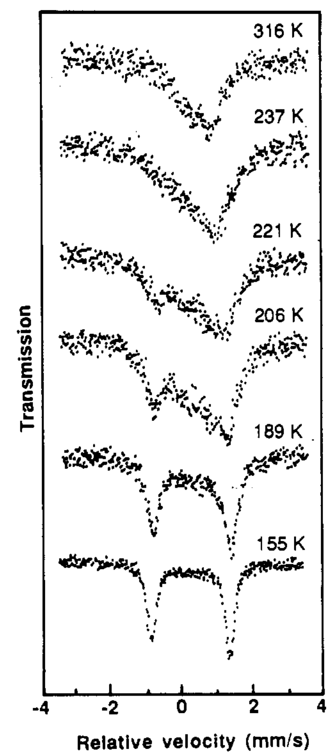

Figure 3. Mössbauer spectra of $[Fe(acpa)_2]PF_6$.

and isotropic thermal parameters for H atoms. Atomic scattering factors and anomalous scattering corrections were taken from ref 40. Crystallographic data and data collection parameters are summarized in Tables I and II. Final atomic parameters for non-hydrogen atoms for both complexes are listed in Tables III and IV. All calculations were carried out on a HITAC M680 computer at the Computer Center of the Institute for Molecular Science with the program system UNICS-III.[41] Additional structural details may be found in the supplementary material.

Results

Magnetic Susceptibility. The temperature dependence of the magnetic susceptibilities was measured for $[Fe(acpa)_2]X$ (X = BPh_4, PF_6). Effective magnetic moments μ_{eff} for the BPh_4^- salt and PF_6^- salt increased gradually from 2.20 and 2.18 μ_B at 78 K to 5.52 μ_B at 320 K and 5.86 μ_B at 300 K, respectively, as the temperature increased. This magnetic behavior indicates an $^6A_1 \rightleftharpoons {}^2T_2$ spin-equilibrium process. The temperature dependence of the fractions f_{HS} of the high-spin species was calculated by using a simple additive property of magnetic susceptibilities as follows:

$$\mu_{eff}^2 = f_{HS}\mu_{eff}(HS)^2 + (1 - f_{HS})\mu_{eff}(LS)^2$$

Here $\mu_{eff}(HS)$ and $\mu_{eff}(LS)$ are effective magnetic moments for high-spin ($S = {}^5/_2$) and low-spin ($S = {}^1/_2$) states, respectively. We adopted the values of 2.18 and 5.92 μ_B for $\mu_{eff}(LS)$ and $\mu_{eff}(HS)$, respectively, which are based on the experimental value at 78 K for the PF_6^- salt and the spin-only value for the $S = {}^5/_2$ state, to calculate f_{HS}. The temperature dependence of f_{HS} is depicted in Figure 1. Both compounds are in the complete low-spin state at 78 K, which has been confirmed by Mössbauer spectra. Their temperature-dependent magnetic behaviors are, however, different, and 97.8% spin interconversion has occurred in the PF_6^- salt at 300 K, while 85.2% of the low-spin species converted to the high-spin state in the BPh_4^- salt at 320 K.

Mössbauer Spectra. ^{57}Fe Mössbauer spectra for $[Fe(acpa)_2]X$ (X = BPh_4, PF_6) have been previously reported.[31] Freshly prepared samples, one of which was used for the X-ray crystallographic analyses, showed the same Mössbauer spectroscopic behavior as that for the previously reported samples. As shown in Figure 2 and 3, the Mössbauer spectra of both compounds at 77 and 300 K show only one quadrupole doublet corresponding to the low- and high-spin states, respectively. The quadrupole splitting and isomer shift parameters are typical for each spin state. In the PF_6^- salt, a new quadrupole doublet, which can be assigned to the high-spin species, is growing as the temperature is raised from liquid-nitrogen temperature; that is, the spectra consist of a superposition of two quadrupole doublets. In contrast to the PF_6^- salt, the BPh_4^- salt shows only one quadrupole doublet with an asymmetric line width at the whole temperature range measured. This asymmetry is observed when the paramagnetic relaxation is not sufficiently rapid relative to the ^{57}Fe nuclear Lamor precession frequency to average the internal magnetic field to zero over the lifetime of the nuclear excited state.[42] The observation of a single quadrupole doublet, when high- and low-spin species coexist, implies a rapid spin-state interconversion rate between the two spin states compared with the inverse of the lifetime of

(40) *International Tables for X-ray Crystallography*; Kynoch Press: Birmingham, England, 1974; Vol. 4.
(41) Sakurai, T.; Kobayashi, K. *Rikagaku Kenkyusho Hokoku* **1979**, *55*, 69.
(42) Blume, M. *Phys. Rev. Lett.* **1965**, *14*, 96.

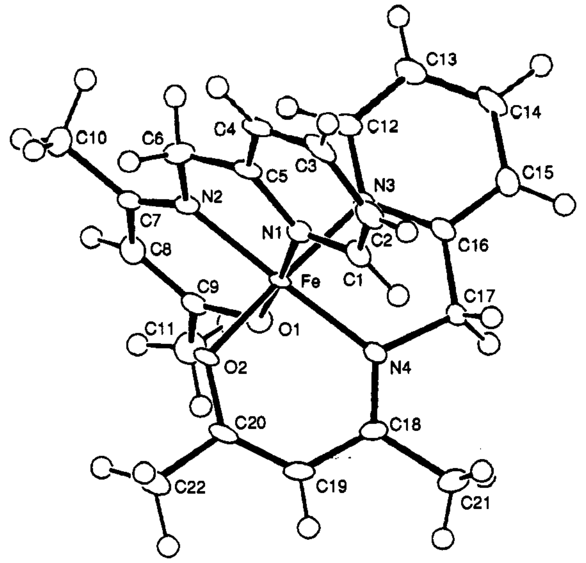

Figure 4. ORTEP drawing of $[Fe(acpa)_2]^+$ of the BPh_4 salt at 120 K.

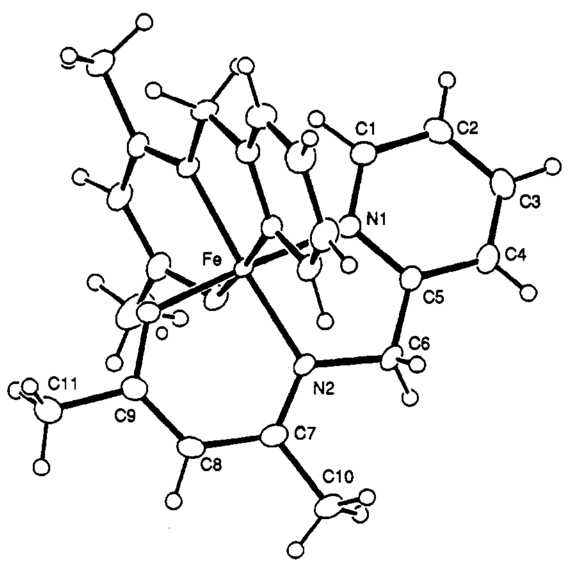

Figure 5. ORTEP drawing of $[Fe(acpa)_2]^+$ of the PF_6 salt at 120 K.

the ^{57}Fe Mössbauer nucleus ($>10^7$ s^{-1}). All spectra of the BPh_4^- salt were analyzed by assuming a single quadrupole doublet, while the spectra of the PF_6^- salt were analyzed with the use of two sets of quadrupole doublets when the spin crossover occurs. The observed Mössbauer parameters are listed in Tables V and VI.

Simulations of the Mössbauer spectra to estimate the relaxation time τ ($\tau = \tau_l\tau_h/(\tau_l + \tau_h)$, where τ_l and τ_h represent the lifetimes of low- and high-spin states, respectively, have already been done.[31,43] The relaxation times are temperature dependent and range from 6.9×10^{-7} to 1.6×10^{-5} and from 1.9×10^{-6} to 3.4×10^{-5} s for the BPh_4^- and PF_6^- salts, respectively. These simulations also support the fact that the spin interconversion for the BPh_4^- salt is faster than that of the PF_6^- salt.

Molecular Structure. The molecular structures of $[Fe(acpa)_2]X$ ($X = BPh_4$, PF_6) were determined at several temperatures. The fraction of high-spin species at each temperatures is listed in Table VII. ORTEP drawings of the molecular structures are depicted in Figures 4 and 5, together with the atomic labeling systems. Counteranions are omitted for clarity. Selected bond lengths and angles are listed in Tables VIII and IX. Stereoviews of the packing diagrams for both salts at 120 K are shown in Figures 6 and 7. Within the temperature range measured, the two complexes do not show any drastic crystallographic change such

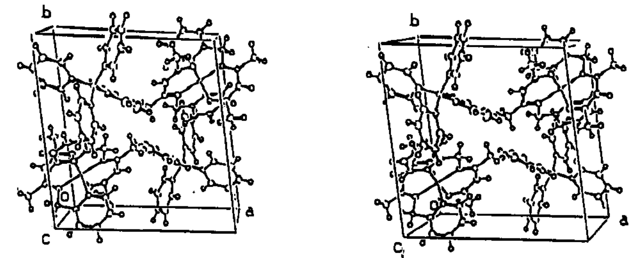

Figure 6. Stereoview of the packing diagram of $[Fe(acpa)_2]BPh_4$ at 120 K.

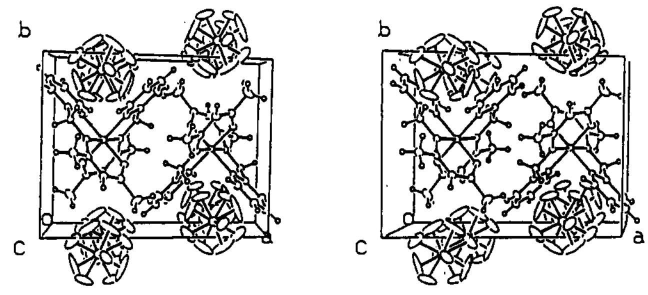

Figure 7. Stereoview of the packing diagram of $[Fe(acpa)_2]PF_6$ at 120 K. The PF_6^- anions are positionally disordered.

as a space group change, which was found in $[Fe(3\text{-}OEt\text{-}SalAPA)_2]ClO_4{\cdot}C_6H_6$,[18] where 3-OEt-SalAPA is the monoanion of the Schiff base condensate of 3-ethoxysalicylaldehyde and *N*-(3-aminopropyl)aziridine. It should be noted that both the PF_6^- and the BPh_4^- salts show a thermochromism; that is, the dark blue color in acetone solution at room temperature turns to green at the liquid-nitrogen temperature.

$[Fe(acpa)_2]BPh_4$. Dark blue crystals of the BPh_4^- salt consist of $[Fe(acpa)_2]^+$ and a counteranion. No positional disorder was found. The iron atoms are pseudooctahedrally coordinated by four N atoms and two O atoms in the cis position: two N atoms of pyridine and two N atoms of imine. Coordination lengths at 120 K (low-spin state) are gradually elongated as the spin state change to the high-spin state. For the BPh_4^- salt, the average bond lengths (Å) at 120 and 311 K, where the low- and high-spin fractions are 96.7 and 80.9%, respectively, are as follows: $Fe\text{–}O_{av} = 1.896$ (3), $Fe\text{–}N(imine)_{av} = 1.938$ (3), and $Fe\text{–}N(pyridine)_{av} = 1.982$ (3) Å at 120 K and $Fe\text{–}O_{av} = 1.917$ (2), $Fe\text{–}N(imine)_{av} = 2.028$ (2), and $Fe\text{–}N(pyridine)_{av} = 2.088$ (2) Å at 311 K. Typical metal to ligand bond lengths for high- and low-spin species are listed in Table X. These values are in good agreement with reported values for typical high- and low-spin species, respectively. As pointed out by Murray et al.[28] and by us,[37] the bond angles around the iron atom are sensitive to the change of spin state. Drastic changes are observed in the Fe–O1–C9 and Fe–O2–C20 angles of these complexes (125.4° at 120 K to 129.1° at 311 K). Such bond angle changes accompanying the M–L bond length changes have also been observed in coordination compounds, e.g. tris(morpholinocarbodithioato)chromium(III), -manganese(III), and -rhodium(III) complexes[44] and Co(II), Co(II), Mn(II), Ni(II), and Zn(II) complexes with (2-nitrophenoxy)ethanoic acid.[45] It should be noted that the coordination geometries around the iron atoms including metal to ligand bond lengths are changed with the spin transition. Dihedral angles between two FeN_2O least-square planes do not show a substantial temperature dependence (Table VIII).

$[Fe(acpa)_2]PF_6$. The crystal structure of the PF_6^- salt at 290 K has already been reported.[43] The dark blue crystals of the PF_6^- salt consist of $[Fe(acpa)^2]^+$ and a counteranion. The geometry around the iron atom is also described as a pseudooctahedron. The $[Fe(acpa)^2]^+$ and PF_6^- ions are located on the crystallographic 2-fold axis, while $[Fe(acpa)_2]^+$ of the BPh_4^- salt has only a

(43) Maeda, Y.; Oshio, H.; Takashima, Y.; Mikuriya, M.; Hidaka, M. *Inorg. Chem.* **1986**, *25*, 2958.
(44) Butcher, R. J.; Sinn, E. *J. Chem. Soc., Dalton Trans.* **1975**, 2571.
(45) Kennard, C. H. L.; Stewart, S. W.; O'Reilly, E. J.; Smith, G.; White, A. H. *Polyhedron* **1985**, *4*, 697.

Table III. Positional (×10[5] for Iron and ×10[4] for the Other Atoms) and Equivalent Isotropic Thermal Parameters (Å[2]) for $[Fe(acpa)_2]BPh_4$

	x	y	z	B_{eq}[a]		x	y	z	B_{eq}[a]		x	y	z	B_{eq}[a]
							(a) At 120 K							
Fe	86939 (4)	75641 (4)	42124 (4)	1.0	C12	7278 (3)	8601 (3)	2481 (3)	1.5	CB21	8035 (3)	2146 (3)	−476 (3)	1.2
O1	8425 (2)	8385 (2)	5460 (2)	1.4	C13	7055 (3)	9342 (3)	1720 (3)	1.9	CB22	8417 (3)	1335 (3)	−966 (3)	1.6
O2	9190 (2)	6574 (2)	5182 (2)	1.3	C14	7893 (3)	10099 (3)	1633 (3)	1.9	CB23	9459 (3)	1132 (3)	−587 (3)	1.8
N1	8865 (2)	6716 (2)	2853 (2)	1.3	C15	8922 (3)	10092 (3)	2306 (3)	1.6	CB24	10188 (3)	1744 (3)	323 (3)	1.9
N2	7271 (2)	6738 (2)	3895 (2)	1.3	C16	9094 (3)	9314 (3)	3013 (3)	1.2	CB25	9833 (3)	2549 (3)	830 (3)	2.0
N3	8282 (2)	8584 (2)	3110 (2)	1.1	C17	10195 (3)	9236 (3)	3712 (3)	1.2	CB26	8794 (3)	2749 (3)	449 (3)	1.3
N4	10109 (2)	8399 (2)	4475 (2)	1.1	C18	10975 (3)	8284 (3)	5241 (3)	1.2	CB31	7016 (3)	3317 (3)	−1902 (3)	1.4
C1	9758 (3)	6762 (3)	2438 (3)	1.5	C19	10975 (3)	7463 (3)	5957 (3)	1.6	CB32	7378 (3)	3066 (3)	−2916 (3)	1.8
C2	9805 (3)	6165 (3)	1459 (3)	1.7	C20	10146 (3)	6657 (3)	5863 (3)	1.4	CB33	7605 (3)	3779 (3)	−3690 (3)	2.1
C3	8872 (4)	5526 (3)	861 (3)	2.0	C21	12039 (3)	8983 (3)	5345 (3)	1.8	CB34	7514 (3)	4794 (3)	−3466 (4)	2.3
C4	7963 (3)	5451 (3)	1305 (3)	1.6	C22	10319 (3)	5771 (3)	6565 (3)	2.0	CB35	7183 (3)	5074 (3)	−2452 (4)	2.2
C5	7974 (3)	6048 (3)	2314 (3)	1.4	B	6819 (3)	2438 (3)	−1008 (3)	1.3	CB36	6940 (3)	4341 (3)	−1710 (3)	1.7
C6	7038 (3)	5975 (3)	2882 (3)	1.8	CB11	6023 (3)	1389 (3)	−1706 (3)	1.3	CB41	6228 (3)	2828 (3)	9 (3)	1.4
C7	6549 (3)	6755 (3)	4531 (3)	1.4	CB12	5466 (3)	1291 (3)	−2880 (3)	1.8	CB42	6570 (3)	2745 (3)	1216 (3)	1.5
C8	6722 (3)	7456 (3)	5528 (3)	1.8	CB13	4878 (3)	359 (3)	−3426 (3)	2.2	CB43	6037 (3)	3084 (3)	2028 (3)	2.0
C9	7602 (3)	8206 (3)	5918 (3)	1.4	CB14	4825 (3)	−494 (3)	−2840 (4)	2.2	CB44	5106 (4)	3507 (3)	1682 (4)	2.4
C10	5485 (3)	6040 (3)	4199 (3)	2.1	CB15	5333 (3)	−424 (3)	−1660 (4)	2.1	CB45	4719 (4)	3558 (4)	503 (4)	3.1
C11	7629 (3)	8931 (3)	6958 (4)	2.3	CB16	5895 (3)	515 (3)	−1124 (3)	1.7	CB46	5274 (3)	3232 (3)	−293 (3)	2.4
							(b) At 202 K							
Fe	86960 (3)	75666 (2)	42082 (3)	1.6	C12	7289 (2)	8613 (2)	2465 (2)	2.3	CB21	8015 (2)	2149 (2)	−489 (2)	1.9
O1	8421 (1)	8378 (1)	5448 (1)	2.2	C13	7077 (2)	9338 (2)	1706 (2)	3.0	CB22	8396 (2)	1336 (2)	−984 (2)	2.4
O2	9197 (1)	6580 (1)	5178 (1)	2.3	C14	7902 (2)	10089 (2)	1624 (2)	3.3	CB23	9438 (2)	1133 (2)	−596 (2)	2.9
N1	8867 (1)	6718 (1)	2852 (2)	1.8	C15	8920 (2)	10079 (2)	2289 (2)	2.6	CB24	10148 (2)	1732 (2)	304 (2)	3.2
N2	7283 (1)	6736 (1)	3882 (2)	1.9	C16	9093 (2)	9312 (2)	3007 (2)	1.9	CB25	9816 (2)	2538 (2)	825 (2)	3.1
N3	8286 (1)	8586 (1)	3105 (2)	1.7	C17	10183 (2)	9232 (2)	3715 (2)	2.1	CB26	8772 (2)	2743 (2)	427 (2)	2.3
N4	10100 (1)	8403 (1)	4468 (2)	1.7	C18	10971 (2)	8280 (2)	5235 (2)	2.1	CB31	7017 (2)	3314 (2)	−1911 (2)	2.0
C1	9762 (2)	6754 (2)	2433 (2)	2.2	C19	10969 (2)	7458 (2)	5940 (2)	2.5	CB32	7366 (2)	3080 (2)	−2919 (2)	2.9
C2	9806 (2)	6170 (2)	1459 (2)	2.7	C20	10147 (2)	6668 (2)	5854 (2)	2.3	CB33	7604 (2)	3788 (2)	−3684 (2)	3.5
C3	8889 (2)	5524 (2)	868 (2)	3.0	C21	12019 (2)	8971 (2)	5336 (2)	3.0	CB34	7509 (2)	4790 (2)	−3447 (3)	3.7
C4	7977 (2)	5458 (2)	1306 (2)	2.7	C22	10325 (2)	5778 (2)	6551 (2)	3.4	CB35	7187 (2)	5062 (2)	−2454 (3)	3.5
C5	7988 (2)	6052 (2)	2309 (2)	2.2	B	6808 (2)	2437 (2)	−1020 (2)	2.0	CB36	6938 (2)	4340 (2)	−1712 (2)	2.7
C6	7051 (2)	5984 (2)	2868 (2)	2.8	CB11	6019 (2)	1405 (2)	−1730 (2)	2.2	CB41	6230 (2)	2824 (2)	−4 (2)	2.1
C7	6564 (2)	6752 (2)	4517 (2)	2.3	CB12	5457 (2)	1311 (2)	−2891 (2)	2.7	CB42	6557 (2)	2743 (2)	1187 (2)	2.5
C8	6734 (2)	7438 (2)	5519 (2)	2.9	CB13	4864 (2)	384 (2)	−3439 (2)	3.6	CB43	6021 (2)	3068 (2)	2002 (2)	3.2
C9	7600 (2)	8193 (2)	5912 (2)	2.4	CB14	4815 (2)	−468 (2)	−2849 (3)	3.7	CB44	5105 (2)	3493 (2)	1658 (3)	4.0
C10	5512 (2)	6035 (2)	4193 (3)	3.5	CB15	5318 (2)	−394 (2)	−1692 (3)	3.5	CB45	4731 (3)	3559 (3)	493 (3)	4.9
C11	7627 (2)	8907 (2)	6954 (2)	3.7	CB16	5890 (2)	528 (2)	−1151 (2)	2.7	CB46	5279 (2)	3234 (2)	−311 (2)	4.0
							(c) At 247 K							
Fe	87005 (3)	75692 (3)	42347 (3)	2.1	C12	7306 (2)	8626 (2)	2471 (2)	3.0	CB21	8011 (2)	2154 (2)	−493 (2)	2.3
O1	8398 (1)	8364 (1)	5469 (1)	3.0	C13	7104 (2)	9353 (2)	1718 (2)	4.0	CB22	8391 (2)	1349 (2)	−980 (2)	3.1
O2	9230 (1)	6599 (1)	5197 (1)	3.3	C14	7922 (2)	10093 (2)	1632 (2)	4.2	CB23	9424 (2)	1141 (2)	−598 (2)	3.7
N1	8855 (1)	6709 (1)	2855 (2)	2.3	C15	8933 (2)	10087 (2)	2299 (2)	3.5	CB24	10126 (2)	1738 (2)	306 (2)	4.1
N2	7270 (2)	6737 (1)	3894 (2)	2.5	C16	9103 (2)	9323 (2)	3017 (2)	2.4	CB25	9797 (2)	2545 (2)	819 (2)	3.9
N3	8297 (2)	8600 (1)	3114 (2)	2.3	C17	10193 (2)	9245 (2)	3722 (2)	2.7	CB26	8762 (2)	2746 (2)	422 (2)	2.9
N4	10117 (1)	8415 (1)	4473 (2)	2.2	C18	10990 (2)	8282 (2)	5214 (2)	2.8	CB31	7022 (2)	3325 (2)	−1901 (2)	2.7
C1	9745 (2)	6744 (2)	2427 (2)	2.8	C19	10996 (2)	7463 (2)	5918 (2)	3.8	CB32	7383 (2)	3104 (2)	−2906 (2)	3.8
C2	9784 (2)	6160 (2)	1457 (2)	3.6	C20	10179 (2)	6679 (2)	5849 (2)	3.3	CB33	7623 (2)	3820 (3)	−3658 (3)	4.6
C3	8871 (3)	5526 (2)	875 (2)	4.0	C21	12030 (2)	8976 (2)	5307 (3)	4.2	CB34	7524 (2)	4803 (2)	−3421 (3)	4.9
C4	7959 (2)	5460 (2)	1315 (2)	3.6	C22	10360 (3)	5792 (2)	6550 (3)	5.1	CB35	7186 (2)	5066 (2)	−2434 (3)	4.5
C5	7973 (2)	6050 (2)	2319 (2)	2.7	B	6811 (2)	2444 (2)	−1019 (2)	2.5	CB36	6933 (2)	4337 (2)	−1698 (2)	3.3
C6	7042 (2)	5991 (2)	2886 (2)	3.6	CB11	6027 (2)	1423 (2)	−1730 (2)	2.7	CB41	6228 (2)	2820 (2)	−3 (2)	2.7
C7	6545 (2)	6754 (2)	4518 (2)	2.9	CB12	5469 (2)	1328 (2)	−2889 (2)	3.6	CB42	6556 (2)	2735 (2)	1188 (2)	3.0
C8	6707 (2)	7437 (2)	5513 (2)	3.8	CB13	4876 (2)	409 (3)	−3438 (2)	4.6	CB43	6011 (2)	3056 (2)	2004 (2)	3.9
C9	7574 (2)	8181 (2)	5925 (2)	3.2	CB14	4819 (2)	−437 (2)	−2848 (3)	4.7	CB44	5103 (3)	3466 (3)	1660 (3)	5.1
C10	5496 (2)	6041 (2)	4183 (3)	4.5	CB15	5314 (2)	−368 (2)	−1690 (3)	4.2	CB45	4731 (3)	3534 (3)	501 (3)	6.1
C11	7608 (3)	8880 (3)	6983 (3)	5.2	CB16	5886 (2)	544 (2)	−1152 (2)	3.3	CB46	5279 (2)	3219 (3)	−305 (3)	4.8
							(d) At 311 K							
Fe	87102 (3)	75758 (3)	43082 (3)	2.9	C12	7346 (2)	8677 (2)	2509 (3)	4.2	CB21	8013 (2)	2175 (2)	−481 (2)	3.0
O1	8337 (1)	8323 (1)	5547 (2)	4.3	C13	7158 (2)	9398 (3)	1759 (3)	5.5	CB22	8395 (2)	1379 (2)	−963 (2)	4.0
O2	9336 (2)	6640 (1)	5275 (2)	4.6	C14	7983 (3)	10138 (3)	1679 (3)	5.8	CB23	9414 (2)	1175 (2)	−576 (3)	5.0
N1	8817 (2)	6684 (1)	2864 (2)	3.2	C15	8979 (2)	10123 (2)	2341 (3)	4.7	CB24	10110 (2)	1761 (3)	309 (3)	5.4
N2	7233 (2)	6738 (2)	3930 (2)	3.4	C16	9136 (2)	9357 (2)	3049 (2)	3.2	CB25	9783 (2)	2558 (2)	821 (3)	5.0
N3	8330 (2)	8646 (1)	3146 (2)	3.1	C17	10219 (2)	9274 (2)	3740 (2)	3.6	CB26	8759 (2)	2758 (2)	424 (2)	3.8
N4	10161 (2)	8440 (1)	4476 (2)	2.9	C18	11054 (2)	8301 (2)	5162 (2)	3.7	CB31	7040 (2)	3348 (2)	−1871 (2)	3.3
C1	9695 (2)	6715 (2)	2411 (2)	3.9	C19	11098 (2)	7483 (2)	5850 (3)	5.1	CB32	7437 (2)	3171 (2)	−2856 (3)	4.9
C2	9709 (3)	6139 (2)	1436 (3)	5.0	C20	10308 (3)	6702 (2)	5850 (2)	4.6	CB33	7690 (3)	3892 (3)	−3597 (3)	6.1
C3	8786 (3)	5517 (2)	875 (3)	5.6	C21	12081 (2)	8986 (3)	5206 (3)	5.9	CB34	7565 (3)	4863 (3)	−3343 (3)	6.1
C4	7899 (3)	5461 (2)	1338 (3)	4.9	C22	10529 (3)	5821 (3)	6536 (3)	7.2	CB35	7176 (3)	5076 (2)	−2377 (3)	5.8
C5	7929 (2)	6049 (2)	2347 (2)	3.7	B	6825 (2)	2459 (2)	−1008 (3)	3.2	CB36	6922 (2)	4338 (2)	−1668 (2)	4.3
C6	7011 (2)	5998 (2)	2927 (3)	4.9	CB11	6048 (2)	1449 (2)	−1723 (2)	3.3	CB41	6224 (2)	2806 (2)	12 (2)	3.4
C7	6487 (2)	6773 (2)	4536 (2)	4.0	CB12	5513 (2)	1361 (2)	−2884 (3)	4.6	CB42	6549 (2)	2729 (2)	1203 (2)	3.9
C8	6626 (2)	7443 (2)	5519 (3)	5.0	CB13	4914 (3)	454 (3)	−3436 (3)	5.9	CB43	5995 (3)	3027 (2)	2013 (3)	5.0
C9	7496 (2)	8160 (2)	5976 (2)	4.4	CB14	4830 (3)	−377 (2)	−2844 (3)	6.0	CB44	5080 (3)	3404 (3)	1670 (3)	6.4
C10	5431 (3)	6079 (3)	4181 (3)	6.4	CB15	5311 (2)	−319 (2)	−1684 (3)	5.4	CB45	4714 (3)	3463 (3)	515 (3)	7.8
C11	7507 (3)	8838 (3)	7029 (3)	7.0	CB16	5887 (2)	575 (2)	−1151 (3)	4.4	CB46	5271 (3)	3174 (3)	−291 (3)	6.1

[a] The equivalent isotropic temperature factor is calculated by using the expression $B_{eq} = (4/3)\sum_i\sum_j \mathbf{a}_i\mathbf{a}_j\beta_{ij}$, where $\mathbf{a}_i$'s are the unit cell edges in direct space.

Table IV. Positional ($\times 10^5$ for Iron at 120 K and $\times 10^4$ for the Other Atoms) and Equivalent isotropic Thermal Parameters ($Å^2$) for $[Fe(acpa)_2]PF_6$[a]

	x	y	z	B_{eq}
		(a) At 120 K		
Fe	75000	47942 (5)	50000	1.0
P	7500	10900 (1)	0	2.0
O	8468 (1)	6139 (2)	6040 (2)	1.5
N1	6465 (1)	3342 (2)	4043 (2)	1.3
N2	6772 (1)	4742 (2)	6317 (2)	1.2
C1	6311 (2)	2776 (2)	2772 (3)	1.6
C2	5554 (2)	1796 (3)	2168 (3)	2.0
C3	4924 (2)	1363 (3)	2901 (3)	2.0
C4	5076 (2)	1949 (3)	4195 (3)	1.9
C5	5848 (2)	2931 (2)	4747 (2)	1.3
C6	6032 (2)	3614 (2)	6127 (2)	1.5
C7	6885 (2)	5618 (2)	7338 (2)	1.4
C8	7592 (2)	6725 (2)	7602 (3)	1.7
C9	8330 (2)	6923 (2)	6985 (3)	1.7
C10	6282 (2)	5425 (3)	8308 (3)	1.9
C11	9070 (2)	8117 (3)	7430 (3)	3.1
F1*	6373 (3)	10174 (4)	−127 (4)	4.4
F2*	7962 (4)	9473 (5)	34 (5)	7.2
F3	7862 (1)	10901 (2)	1684 (2)	3.2
F4*	8521 (3)	11634 (7)	274 (4)	7.8
F5*	8101 (4)	12307 (3)	−93 (4)	4.2
		(b) At 205 K		
Fe	7500	4799 (1)	5000	1.7
P	7500	10874 (1)	0	3.1
O	8439 (1)	6135 (2)	6136 (2)	2.9
N1	6426 (2)	3285 (2)	4065 (2)	2.2
N2	6734 (1)	4686 (2)	6346 (2)	2.0
C1	6288 (2)	2699 (3)	2815 (3)	2.7
C2	5530 (2)	1732 (3)	2236 (3)	3.6
C3	4895 (3)	1333 (3)	2952 (4)	3.9
C4	5027 (2)	1929 (3)	4223 (3)	3.4
C5	5802 (2)	2899 (3)	4754 (3)	2.3
C6	5979 (2)	3583 (3)	6124 (3)	2.5
C7	6846 (2)	5528 (3)	7395 (3)	2.6
C8	7561 (2)	6621 (3)	7710 (3)	3.3
C9	8301 (2)	6866 (3)	7107 (3)	3.2
C10	6224 (2)	5331 (3)	8330 (3)	3.3
C11	9036 (3)	8054 (4)	7582 (5)	5.7
F1*	6313 (4)	10331 (5)	−153 (4)	5.8
F2*	7790 (8)	9373 (5)	35 (11)	8.8
F3	7799 (2)	10875 (2)	1654 (2)	5.2
F4*	8570 (4)	11418 (8)	330 (5)	9.7
F5*	7978 (4)	12351 (4)	−136 (5)	6.7

[a] An asterisk indicates a disordered atom.

Table V. Mössbauer Parameters of $[Fe(acpa)_2]BPh_4$

temp, K	IS, mm/s	QS, mm/s	Γ_+,[a] mm/s	Γ_-,[b] mm/s
78	0.217	2.288	0.376	0.327
110	0.209	2.273	0.340	0.300
128	0.206	2.260	0.337	0.303
142	0.199	2.260	0.322	0.293
160	0.194	2.246	0.340	0.303
171	0.189	2.232	0.330	0.299
189	0.174	2.181	0.425	0.384
205	0.166	2.140	0.505	0.419
229	0.159	2.038	0.674	0.538
253	0.165	1.805	0.991	0.771
268	0.163	1.693	1.107	0.703
286	0.215	1.190	1.411	0.726
293	0.256	1.052	1.466	0.674
317	0.402	0.546	1.616	0.466

[a] Full width at half-maximum (fwhm) for high-energy line. [b] Fwhm for low-energy line.

pseudo-2-fold axis. Four fluorine atoms of the PF_6^- ion are positionally or rotationally disordered around a F–P–F axis. The coordination bond lengths show a temperature dependence similar to that in the BPh_4^- salt. The average bond lengths (Å) (Fe–O = 1.889 (2); Fe–N(pyridine) = 1.989 (2); Fe–N(imine) = 1.941 (2)) at 120 K increase to the typical values for the high-spin species (Fe–O = 1.939 (2); Fe–N(pyridine) = 2.153 (2); Fe–N(imine) = 2.081 (2)) at 290 K (Table IX). Bond angle changes around the iron show the same temperature dependence as in the BPh_4^- salt. In the spin-crossover FeN_4O_2 system studied here, it is clear that the Fe–N(pyridine and imine) bond lengths show a drastic change (0.09–0.164 Å) with the spin interconversion, while the changes of the Fe–O bond lengths are small (0.020–0.040 Å). This tendency can be confirmed in other spin-crossover systems (Table X).

Discussion

In the iron(III) spin-crossover system, the ground state is $^2T_{2g}$ in the approximation of O_h symmetry at low enough temperature, while the $^6A_{1g}$ state becomes the ground state by virtue of the dominant entropy term in the Gibbs free energy at high temperature. As stated in the Introduction, the spin-crossover system is categorized into the "spin-transition (ST)" and "spin-equilibrium (SE)" types depending on the spin-transition behavior. Some iron(III) SE type complexes have rapid spin-interconversion rates compared with the reciprocal of the ^{57}Fe Mössbauer lifetime, giving a single quadrupole doublet in the Mössbauer spectra even at the spin-transition temperatures. The question as to why the spin transitions occur gradually in the SE type complexes has previously been discussed by us.[24] From the temperature dependence of the heat capacity of $[Fe(acpa)_2]PF_6$,[24] the number of molecules in a cell or a domain (domain size n) was estimated to be 5. This value is extremely small compared with the values (95 and 77) for the ST type ferrous complexes $[Fe(phen)_2(NCS)_2]$[10] and $[Fe(phen)_2(NCSe)_2]$,[11] respectively. The small number of molecules in the domain means that the cooperativity of the spin interconversion is much weaker in the SE type than in the ST type complexes and the effect of a spin-state interconversion in a given domain upon the adjacent cells would also be very weak in the SE type complexes. This leads to a rapid fluctuation between low- and high-spin states, hence, the spin interconversion within a wide temperature range.

The next question is why some SE type iron(III) complexes do show a rapid spin interconversion and others do not. There are basically three factors that might be responsible for this phenomenon: (i) a strong interaction between $^2T_{2g}$ and $^6A_{1g}$ states through an excited $^4T_{1g}$ state; (ii) some vibrational modes with an anharmonicity, which may affect the effectiveness of nuclear tunnelling; (iii) structural difference such as reduced metal–ligand bond lengths between two spin states. In this section we address the third factor, that is, intramolecular change accompanying the spin interconversion, to explain the rapid interconversion behavior using structural parameters for $[Fe(acpa)_2]X$ (X = BPh_4, PF_6). We do this for the following reasons. (i) The domain size of the PF_6^- salt was estimated to be n = 5. The temperature dependence of the magnetic susceptibilities of the BPh_4^- salt shows a more gradual spin interconversion as the temperature changes than in the PF_6^- salts (Figure 1). From these experimental results, it can be expected that the domain size in the BPh_4^- salt is even smaller than that in the PF_6^- salt (n = 5). Because of the very small domain size and the weak cooperativity (intermolecular interaction or lattice phonon changes), a small interdomain interaction in both salts is expected. (ii) The entropy arising from the spin interconversion was estimated to be 36.19 J K^{-1} mol^{-1} for the PF_6^- salt from the heat capacity measurements.[24] The transition entropy consists mainly of three contributions: (a) a change in the spin manifold between the low- and high-spin states; (b) a change in the phonon system including both metal to ligand bond length changes and lattice phonons; (c) an order–disorder phenomenon of the solvate molecules and the counterions. Neither the PF_6^- nor the BPh_4^- salts have solvent molecules and the X-ray structural analysis shows that the order–disorder changes do not occur, so we need not take contribution c into account. We measured the temperature dependence of the IR and Raman spectra,[24] and drastic changes were assigned to skeletal vibrational modes of a six-coordinated iron core. The phonon entropy due to the skeletal vibrational changes accompanying the spin interconversion was estimated to be 28.56 J K^{-1} mol^{-1}. The observed entropy gain,

Table VI. Mössbauer Parameters of $[Fe(acpa)_2]PF_6$

	high-spin component				low-spin component				
temp, K	IS mm/s	QS mm/s	Γ_+, mm/s	Γ_-, mm/s	IS, mm/s	QS, mm/s	Γ_+, mm/s	Γ_-, mm/s	S,[a] %
81	0.248	2.236	0.315	0.306					0.0
104	0.246	2.232	0.324	0.314					0.0
130	0.245	2.206	0.300	0.289					0.0
155	0.233	2.190	0.317	0.329					0.0
189	0.208	2.167	0.389	0.389	0.571	0.895	1.283	0.798	42.2
206	0.202	2.105	0.549	0.422	0.446	0.815	1.102	1.069	66.9
221	0.203	1.983	0.627	0.627	0.361	0.762	1.058	0.793	61.6
237	0.202	2.100	0.236	0.236	0.378	0.805	1.539	0.802	95.4
261					0.291	0.740	1.077	0.919	100.0
283					0.330	0.663	0.894	0.801	100.0
316					0.333	0.636	1.046	0.614	100.0

[a] High-spin fraction.

Table VII. High-Spin Fractions (f_{HS}) at the Temperatures of X-ray Measurements

$[Fe(acpa)_2]BPh_4$		$[Fe(acpa)_2]PF_6$	
temp, K	f_{HS}, %	temp, K	f_{HS}, %
120	3.3	120	3.9
202	12.7	205	54.1
247	34.1	290	97.7
311	80.9		

Table VIII. Temperature Dependences of Bond Lengths (Å), bond Angles (deg), and Dihedral Angles (deg) of $[Fe(acpa)_2]BPh_4$

	120 K	202 K	247 K	311 K
Fe–O1	1.902 (3)	1.896 (2)	1.913 (2)	1.920 (2)
Fe–O2	1.889 (3)	1.891 (2)	1.873 (2)	1.913 (2)
Fe–N1	1.976 (3)	1.979 (2)	2.022 (2)	2.082 (2)
Fe–N2	1.937 (3)	1.941 (2)	1.971 (2)	2.027 (2)
Fe–N3	1.987 (3)	1.990 (2)	2.001 (2)	2.093 (2)
Fe–N4	1.938 (3)	1.939 (2)	1.969 (2)	2.029 (2)
O1–Fe–O2	93.5 (1)	93.6 (1)	94.5 (1)	95.2 (1)
O1–Fe–N1	175.8 (1)	175.6 (1)	174.1 (1)	169.6 (1)
O1–Fe–N2	93.5 (1)	93.8 (1)	93.4 (1)	90.5 (1)
O1–Fe–N3	90.9 (1)	90.9 (1)	90.8 (1)	91.8 (1)
O1–Fe–N4	87.7 (1)	87.8 (1)	88.8 (1)	94.0 (1)
O2–Fe–N1	89.2 (1)	89.0 (1)	88.4 (1)	88.5 (1)
O2–Fe–N2	87.5 (1)	87.5 (1)	89.4 (1)	94.3 (1)
O2–Fe–N3	174.5 (1)	174.3 (1)	172.6 (1)	168.1 (1)
O2–Fe–N4	94.0 (1)	94.1 (1)	93.1 (1)	90.6 (1)
N1–Fe–N2	83.4 (1)	82.7 (1)	81.4 (1)	79.5 (1)
N1–Fe–N3	86.6 (1)	86.8 (1)	86.9 (1)	86.2 (1)
N1–Fe–N4	95.4 (1)	95.6 (1)	96.2 (1)	95.7 (1)
N2–Fe–N3	95.6 (1)	95.8 (1)	95.4 (1)	95.2 (1)
N2–Fe–N4	178.1 (1)	177.7 (1)	176.5 (1)	173.0 (1)
N3–Fe–N4	82.8 (1)	82.4 (1)	81.8 (1)	79.3 (1)
Fe–O1–C9	125.3 (1)	125.4 (1)	126.0 (2)	129.2 (2)
Fe–O2–C20	125.5 (2)	125.2 (1)	126.0 (2)	129.0 (2)
Fe–N1–C1	125.8 (2)	126.1 (1)	125.7 (1)	124.9 (2)
Fe–N1–C5	115.0 (3)	115.6 (2)	116.2 (2)	116.2 (2)
Fe–N2–C6	115.0 (3)	115.4 (2)	115.9 (2)	116.0 (2)
Fe–N2–C7	126.4 (2)	125.9 (1)	125.6 (2)	125.8 (2)
Fe–N3–C12	125.5 (2)	126.1 (2)	125.8 (2)	125.3 (2)
Fe–N3–C16	115.5 (2)	115.7 (1)	115.5 (2)	116.3 (2)
Fe–N4–C17	115.4 (2)	115.7 (1)	116.0 (1)	116.7 (1)
Fe–N4–C18	126.3 (3)	125.9 (2)	126.2 (2)	125.9 (2)
dihedral angles[a]	89.80 (8)	89.86 (5)	89.56 (6)	90.08 (6)

[a] Dihedral angles between two FeN_2O least-squares planes.

36.19 J K^{-1} mol^{-1}, arising from spin interconversion can be explained by the sum of the change in the spin manifold (9.13 J K^{-1} mol^{-1}) and the skeletal normal mode (28.56 J K^{-1} mol^{-1}). Therefore, it can be expected that the contribution of lattice phonon changes in the SE system to the spin interconversion is very small.

Bond length changes as the result of the spin interconversion for various SE type iron(III) complexes are listed in Table X. From the plot of bond lengths vs high-spin fractions (f_{HS}) shown in Figure 8, the bond lengths are almost linearly correlated to the f_{HS} values. In order to compare the bond lengths in the high- and low-spin states for the BPh_4^- and the PF_6^- salts, the values for pure high-spin species for both salts were estimated by a linear

Table IX. Temperature Dependence of Selected Intramolecular Bond Distances (Å), Bond Angles (deg), and Dihedral Angles (deg) of $[Fe(acpa)_2]PF_6$[a]

	120 K	205 K	290 K[b]
Fe–O	1.889 (2)	1.914 (2)	1.939 (2)
Fe–N1	1.989 (2)	2.071 (2)	2.153 (2)
Fe–N2	1.941 (2)	2.010 (2)	2.081 (2)
O–Fe–N1	175.6 (1)	170.5 (1)	166.0 (1)
O–Fe–N2	93.5 (1)	91.2 (1)	89.0 (1)
N1–Fe–N2	82.4 (1)	79.7 (1)	77.5 (1)
O–Fe–O*	91.0 (1)	92.9 (1)	94.2 (1)
O–Fe–N1*	90.6 (1)	90.5 (1)	91.1 (1)
O–Fe–N2*	88.6 (1)	93.2 (1)	97.1 (1)
N1–Fe–N1*	88.1 (1)	87.6 (1)	86.8 (1)
N1*–Fe–N2	95.5 (1)	95.7 (1)	96.0 (1)
N2–Fe–N2*	177.0 (1)	173.7 (1)	171.1 (1)
Fe–O–C9	124.5 (2)	126.8 (2)	129.4 (2)
Fe–N1–C1	126.4 (2)	125.4 (2)	124.9 (2)
Fe–N1–C5	115.0 (2)	116.0 (2)	116.3 (2)
Fe–N2–C6	115.7 (2)	116.5 (2)	117.1 (2)
Fe–N2–C7	126.1 (2)	125.8 (2)	125.5 (2)
dihedral angles[c]	89.26 (4)	89.66 (5)	89.38 (4)

[a] Key to a symmetry operation: asterisk indicates coordinates $^3/_2 - x$, y, $1 - z$. [b] Reference 43. [c] Dihedral angle between two FeN_2O least-squares planes.

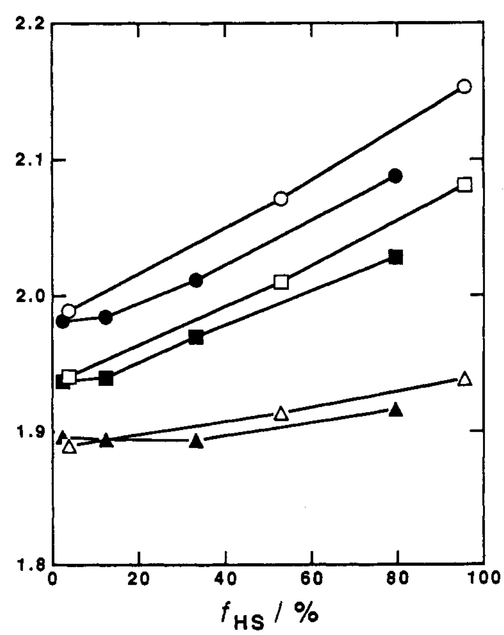

Figure 8. Plot of coordination bond lengths vs high-spin fraction: (i) Fe–N(pyridine)$_{av}$ (●), Fe–N(imine)$_{av}$ (■), and Fe-O (▲) for $[Fe(acpa)_2]BPh_4$; (ii) Fe–N(pyridine) (○), Fe–N(imine) (□), and Fe–O (△) for $[Fe(acpa)_2]PF_6$.

Table X. Coordination Bond Lengths (Å) and Their Differences for High- and Low-Spin Species of Spin-Crossover Complexes with Schiff Bases as Ligands[a]

	high spin low spin			bond difference			
	Fe–O	Fe–N_{py}	Fe–N_{im}	ΔFe–O	ΔFe–N_{py}	ΔFe–N_{im}	ref
$[Fe(acpa)_2]BPh_4$	1.916	2.088	2.028	0.020	0.106	0.090	this work
	(1.920)	(2.113)	(2.052)	(2.024)	(0.131)	(0.114)	
	1.896	1.982	1.938				
$[Fe(acpa)_2]PF_6$	1.939	2.153	2.081	0.040	0.164	0.140	this work
	(1.941)	(2.159)	(2.086)	(0.042)	(0.170)	(0.145)	
	1.899	1.989	1.941				
$[Fe(bzpa)_2]ClO_4$	1.921	2.074	2.017	0.013	0.098	0.097	34
	1.908	1.976	1.920				
$[Fe(acen)(3,4\text{-lut})_2]BPh_4$	1.929	2.185	2.057	0.023	0.149	0.139	34
	1.906	2.036	1.918				
$[Fe(3\text{-OEt-SalAPA})]ClO_4$	1.921	2.176	2.085	0.064	0.148	0.128	15
	1.857	2.028	1.957				
$[Fe(im)_2(salen)]ClO_4$	1.901	2.146	2.067	−0.002	0.154	0.154	25
	1.903	1.992	1.913				
$Fe(3\text{-al-SalBzen})_2]NO_3$[b]	1.896	2.121	1.982				41
	1.883	2.047	1.936				

[a] The values in the parentheses are obtained by the linear extrapolation to be 100% high-spin species. The high-spin fractions, which are estimated from the magnetic susceptibility data, are 79.6% for $[Fe(acpa)_2]BPh_4$ at 311 K and 95.5% for $[Fe(acpa)_2]PF_6$ at 290 K, respectively. Ligand abbreviations: bzpa = *N*-(1-benzoyl-2-propylidene)(2-pyridylmethyl)amine; 3,4-lut = 3,4-lutidine; 3-OEt-SalAPA = Schiff base condensate of 3-ethoxysalicylaldehyde and *N*-(3-aminopropyl)aziridine; im = imidazole; salen = *N,N'*-ethylenebis(salicylaldimine); 3-al-SalBzen = Schiff base condensate of *N*-benzylethylenediamine and 3-allylsalicylaldehyde. [b] High-spin fraction is expected to be 33% at room temperature.

extrapolation of the values at the temperature measured to those at 100% high-spin species. Extrapolated values are listed in parentheses in Table X and are used in the following discussion. It should be noted that the magnitudes of bond length changes for the faster spin-interconversion complex BPh_4^- salt is smaller than those of the more slowly interconverting PF_6^- salt: $\Delta\text{Fe–O}_{av}$ = 0.024, $\Delta\text{Fe–N(pyridine)}_{av}$ = 0.131, and $\Delta\text{Fe–N(imine)}_{av}$ = 0.114 Å for the BPh_4^- salt and ΔFe–O = 0.042, $\Delta\text{Fe–N(pyridine)}_{av}$ = 0.170, and $\Delta\text{Fe–N(imine)}_{av}$ = 0.145 Å for the PF_6^- salt. The coordination bond lengths for the low-spin state do not show any significant differences. Therefore, the metal to ligand bond lengths for the pure high-spin states are smaller in the BPh_4^- salt than in the PF_6^- salt: Fe–O_{av} = 1.920, $\text{Fe–N(pyridine)}_{av}$ = 2.113, and Fe–N(imine)_{av} = 2.052 Å for the BPh_4^- salt and Fe–O = 1.941; Fe–N(pyridine) = 2.159, and ΔFe–N(imine) = 2.086 Å for the PF_6^- salt. Let us consider the energy diagrams of the high- and low-spin states at a certain temperature where both BPh_4^- and PF_6^- salts are in the spin-equilibrium state. Ground (low-spin state: $^2T_{2g}$) and excited (high-spin state: $^6A_{1g}$) states are expressed as single parabolic functions. If we assume that the ground states for both complexes have the same energy, the excited $^2T_{2g}$ state for the PF_6^- salt is always placed below the $^2T_{2g}$ state of the BPh_4^- salt because the magnetic susceptibility measurements show that the high-spin fraction of the PF_6^- salt is always higher than that of the BPh_4^- salt at any temperature. If the longer bond lengths of high-spin species for the PF_6^- salt compared to those for the BPh_4^- salts are taken into account, the potential surface of the $^2T_{2g}$ state for the PF_6^- salt is placed further from the $^6A_{1g}$ state than that of the BPh_4^- salt, as shown in Figure 9. That is to say, the activation energy ΔE_a of the spin interconversion for the PF_6^- salt is larger than that of the BPh_4^- salt as a result of the longer bond lengths for the PF_6^- salt. From the Arrhenius equation, the rate constant k for the spin-interconversion phenomena can be related to the activation energy ΔE_a as follows:

$$k = A \exp(-\Delta E_a/RT)$$

Here A and R are the frequency factor and the gas constant, respectively. According to the above arguments, the activation energy ΔE_a of the BPh_4^- salt can be expected to be smaller than that of the PF_6^- salt; hence, it can be concluded that the smaller ΔE_a value for the BP_4^- salt implies the rapid spin interconversion compared with the PF_6^- salt.

Conclusion

The motivation to start this work was to answer the question about why some spin-crossover complexes show a rapid spin in-

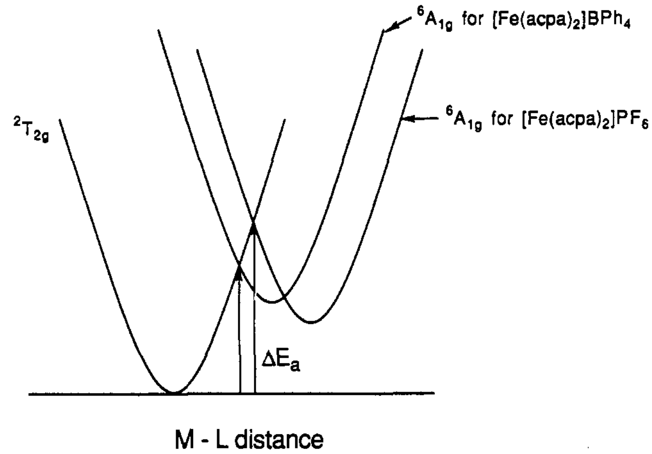

Figure 9. Potential energy diagrams of spin-crossover complexes.

terconversion compared with the ^{57}Fe Mössbauer lifetime (10^{-7} s) and others do not. Mössbauer spectroscopic experiments of $[Fe(acpa)_2]X$ (X = BPh_4, PF_6) revealed that both salts belong to the spin equilibrium (SE) type and the spin interconversion of the BPh_4^- salts is faster than that of the PF_6^- salt. Some spin-interconversion rates in both solution and solid states have already been determined in some ferric spin-crossover complexes,[46-48] and it was proved that spin interconversion in solution is much faster than that of corresponding solid samples. Furthermore, grinding and dilution experiments for the ferric spin-crossover complexes revealed that such physical treatments affect the dynamics of the spin-crossover phenomena.[17,49-52] It is clear that the intermolecular interaction including a lattice phonon coupling is the cause for different dynamics in the spin-crossover behavior. However, taking into account the very small domain size (small cooperativity) of both salts, the different spin-inter-

(46) Petty, R. H.; Dose, E. V.; Tweedle, M. F.; Wilson, L. J. *Inorg. Chem.* **1978**, *17*, 1064.
(47) Tweedle, M. F.; Wilson, L. J. *J. Am. Chem. Soc.* **1976**, *98*, 4824.
(48) Dose, E. V.; Murphy, K. M.; Wilson, L. J. *Inorg. Chem.* **1976**, *15*, 2622.
(49) Hadded, M. S.; Federer, W. D.; Lynch, M. W.; Hendrickson, D. N. *Inorg. Chem.* **1981**, *20*, 131.
(50) Hadded, M. S.; Federer, W. D.; Lynch, M. W.; Hendrickson, D. N. *J. Am. Chem. Soc.* **1980**, *102*, 1468.
(51) Federer, W. D.; Hendrickson, D. N. *Inorg. Chem.* **1984**, *23*, 3861.
(52) Timken, M. D.; Hendrickson, D. N.; Sinn, E. *Inorg. Chem.* **1985**, *24*, 3947.

conversion rates in the system studied here can be explained by intramolecular phenomena that might result from the intermolecular effects such as packing differences. X-ray crystallographic analyses of both salts at different temperatures showed that the faster spin interconversion is accompanied by smaller metal to ligand bond length changes in the BPh_4^- salt as compared to the PF_6^- salt. We conclude that the activation energy ΔE_a for the BPh_4^- salt is smaller than that for the PF_6^- salt, and this implies the more rapid spin interconversion in the BPh_4^- salt.

Acknowledgment. We thank Prof. P. Gütlich (Johannes Gutenberg-Universität) and Prof. M. Sorai (Osaka University) for their helpful discussions.

Supplementary Material Available: Tables SI–SXXV, listing X-ray data collection parameters, derived hydrogen positions, thermal parameters, bond distances and angles, and magnetic susceptibility data, and Figures SI–SX, showing molecular structures and packing diagrams (32 pages); tables of calculated and observed structure factors (63 pages). Ordering information is given on any current masthead page.

Contribution from the Department of Chemical Engineering, University of Patras, and Institute of Chemical Engineering and High Temperature Chemical Processes, P.O. Box 1239, GR-26110 Patras, Greece, and Department of Chemistry, Bergakademie Freiberg, D-O-9200 Freiberg, Germany

Thermal Analysis and Raman Spectroscopic Measurements on the Scandium Iodide–Cesium Iodide System

M. M. Metallinou,[1a] L. Nalbandian,[1a] G. N. Papatheodorou,*[,1a] W. Voigt,[1b] and H. H. Emons[1b]

Received March 14, 1991

The phase diagram of the ScI_3–CsI system has been determined and the existence of two solid compounds, Cs_3ScI_6 and $Cs_3Sc_2I_9$, has been established. The Raman spectra of molten ScI_3–CsI mixtures containing up to 60 mol % ScI_3 have been measured at temperatures up to 700 °C. The temperature dependence of the Raman spectra of polycrystalline Cs_3ScI_6 and $Cs_3Sc_2I_9$ compounds from ambient temperatures to temperatures above melting have also been measured. The data are discussed in terms of the possible species formed in the melt mixtures. It is suggested that two predominant ionic species in equilibrium, $ScI_6^{3-} \rightleftharpoons ScI_4^- + 2I^-$, prevail in the melt. A third binuclear Sc species is also present at high ScI_3 concentrations. The Raman frequencies attributed to the ionic species are as follows: for ScI_6^{3-}, $\nu_1 = 119 \pm 1$ cm^{-1}, $\nu_2 = 67 \pm 2$ cm^{-1} ($\nu_5 \approx 80$ cm^{-1}); for ScI_4^-, $\nu_1 = 129 \pm 1$ cm^{-1}, $\nu_2 = 37 \pm 3$ cm^{-1}, $\nu_4 = 54 \pm 3$ cm^{-1}. The Raman spectra of vapors over an equimolar ScI_3–CsI mixture have been measured at 800 °C, and the observed bands at 127 ± 1 and 153 ± 1 cm^{-1} were assigned to the ν_1 stretching frequencies of the ScI_4 tetrahedra in the $CsScI_4$(g) molecule and of the ScI_3(g) molecule, respectively.

Introduction

The structural and thermodynamic properties of binary melts of the type MX_3–AX (X = halide, A = alkali metal, M = trivalent metal) are strongly dependent on the physicochemical properties of the trivalent salts.[2] Studies of binaries containing high-melting MX_3 salts are very limited, mainly due to experimental difficulties. Lanthanide and actinide halides, including the halides of yttrium and scandium, belong to this category. The practical interest for studying these mixtures arises from their use as additives in high-intensity-discharge mercury lamps.[3]

Phase diagrams for most of the above systems are available.[4–6] Calorimetric enthalpies of mixing and/or emf measurements have been performed on the systems YCl_3–ACl,[7] $LaCl_3$–ACl,[8,9] $CeCl_3$–ACl,[9,10] $GdCl_3$–ACl[11] (A = Li, Na, K, Rb, Cs) and $PrCl_3$–ACl[12] (A = Na, K). The results indicate that $LnCl_6^{3-}$ species stabilize the melt in the alkali-metal halide rich region for A = K, Rb, and Cs. Enthalpies of mixing have also been obtained for $LnCl_3$–NaCl (Ln = La, Ce, Nd, Sm, Dy, Er, Yb),[11] as well as $NdBr_3$–NaBr and NdI_3–NaI systems.[11] Electrical conductivity measurements of the LnX_3–AX (A = Na, K, Cs) mixtures indicate "complex" formation at the concentration of the compounds shown in the corresponding phase diagrams.[13,14] Further information for understanding the melt structure is given by combining thermodynamic measurements with spectroscopic techniques.[2] Thus Raman spectroscopic studies on the systems YCl_3–ACl (A = Cs, K, Li),[15] $LaCl_3$–KCl,[16,17] and $LaCl_3$–CsCl[17] have provided concrete evidence for the formation of YCl_6^{3-} and $LaCl_6^{3-}$ configurations in alkali-metal chloride rich mixtures.

This work was aimed at investigating the thermodynamic and structural properties of the ScI_3–CsI system. The phase diagram has been calculated from DTA measurements, and the Raman spectra of the liquid mixtures and the solid compounds formed have been measured at various temperatures.

Experimental Section

Scandium iodide was kindly provided by Dr. T. Russel of General Electric (Cleveland, OH) and used without further treatment. Cesium iodide was purchased from Fluka and was further dehydrated by heating at 100 °C under vacuum for several hours. All anhydrous materials were handled in sealed fused silica containers and/or in an inert atmosphere of a glove box having water content of less than 1 ppm.

For the DTA measurements, almost identical containers made of vitreous silica tubing (6 mm o.d., 4 mm i.d.) were used. The appropriate salt mixture with a total mass of about 80 mg was added, and the container was sealed under vacuum with the use of a propane/oxygen torch. The total length of each sealed container was approximately 12 mm. A similar empty container was used as a reference sample. DTA mea-

(1) (a) University of Patras and ICE/HT. (b) Bergakademie Freiberg.

(2) (a) Brooker, H. M.; Papatheodorou, G. N. In *Advances in Molten Salt Chemistry*, Mamantov, G., Ed.; Elsevier: New York, 1983; Vol. 5, pp 27–165. (b) Papatheodorou, G. N. In *Comprehensive Treatise of Electrochemistry*; Conway, B. E.; Bockris, J. O'M.; Yeager, E., Eds.; Plenum Press: New York, 1983; Vol. 5, pp 399–461.
(3) Van Erk, W.; Rietveld, T. *Philips J. Res.* **1987**, *42*, 102.
(4) *Phase Diagrams for Ceramists*; The American Ceramic Society: Westerville, OH, 1983; Vol. V.
(5) Kutscher, J.; Schneider, A. Z. *Anorg. Allg. Chem.* **1974**, *408*, 135.
(6) Krokhina, A. G.; Andrachnikova, A. P.; Strekachinskij, A. B.; Krokhin, V. A. *Zh. Neorg. Khim.* **1980**, *25*, 1624; *Russ. J. Inorg. Chem. (Engl. Transl.)* **1980**, *25*, 901.
(7) Papatheodorou, G. N.; Woernes, O.; Østvold, T. *Acta Chem. Scand.* **1979**, *A33*, 173.
(8) Papatheodorou, G. N.; Østvold, T. *J. Phys. Chem.* **1974**, *78*, 181.
(9) Papatheodorou, G. N.; Kleppa, O. J. *J. Phys. Chem.* **1974**, *78*, 176.
(10) Egan, J. J.; Bracker, J. *J. Chem. Thermodyn.* **1974**, *6*, 9.
(11) Dienstbach, F.; Blachnik, R. *Z. Anorg. Allg. Chem.* **1975**, *412*, 97.
(12) Iwadate, Y.; Igarashi, K.; Mochinaga, J. *J. Electrochem. Soc.* **1986**, *133*, 1162.
(13) Kutscher, J.; Schneider, A. *Z. Anorg. Allg. Chem.* **1972**, *389*, 157.
(14) Foerthmann, R.; Vogel, G.; Schneider, A. *Z. Anorg. Allg. Chem.* **1969**, *367*, 19.
(15) Papatheodorou, G. N. *J. Chem. Phys.* **1977**, *66*, 2893.
(16) Maroni, V. A.; Hathaway, E. J.; Papatheodorou, G. N. *J. Phys. Chem.* **1974**, *78*, 1134.
(17) Papatheodorou, G. N. *Inorg. Nucl. Chem. Lett.* **1975**, *11*, 483.

0020-1669/91/1330-4260$02.50/0